

# Time dependent simulations of electron transport through a quantum ring: effect of the Lorentz force

B. Szafran<sup>1,2</sup> and F.M. Peeters<sup>1</sup>

<sup>1</sup>*Departement Fysica, Universiteit Antwerpen (Campus Drie Eiken),  
Universiteitsplein 1, B-2610 Antwerpen, Belgium*

<sup>2</sup>*Faculty of Physics and Applied Computer Science,*

*AGH University of Science and Technology, al. Mickiewicza 30, 30-059 Kraków, Poland*

(Dated: December 2, 2024)

The time dependent Schrödinger equation for an electron passing through a semiconductor quantum ring of nonzero width is solved in the presence of a perpendicular homogenous magnetic field. The well-known Aharonov-Bohm oscillations are found in the transmission probability with an amplitude decreasing with increasing magnetic field. The decrease is due to the Lorentz force producing an imbalance in the injection of the electron in the two arms. Furthermore, we discuss the effect of asymmetry in the ring arms introduced by a shallow quantum well. For a quantum well tuned to shift maximally the phase of the maximum of the wave packet we observe a  $\pi$  shift of the Aharonov-Bohm oscillations. For other well depths the oscillations with a period of half of the flux quantum are observed. The time evolution in the presence of the Lorentz force is discussed in the context of microreversibility relations.

PACS numbers: 73.63.Kv

## I. INTRODUCTION

The wave function of an electron passing along a path  $l$  acquires a phase shift<sup>1</sup> from the vector potential  $\mathbf{A}$  given by  $\phi = (2\pi/\Phi_0) \int_l \mathbf{A} \cdot d\mathbf{x}$  ( $\Phi_0 = h/e$  is the flux quantum). In a ring configuration the Aharonov Bohm (AB) effect produces a measurable interference<sup>1</sup> due to the relative phase shifts of the wave function going through both arms  $\Delta\phi = 2\pi\Phi/\Phi_0$ , where  $\Phi$  is the magnetic field flux through the area inside the ring. The oscillations of the electric properties with period  $\Phi_0$  were detected in metal<sup>2</sup> and semiconductor rings.<sup>3,4,5</sup> In disordered metal rings a  $\Phi_0/2$  period of the AB oscillations was expected.<sup>6</sup> Due to elastic scattering the electron wave function passing through the left and right arms meet at the exit of the ring with random relative phases. However, the scattering phase shifts cancel out for paths circulating left and right and meeting at the lead of their origin. For fluxes equal to integer multiples of  $\Phi_0/2$  a constructive interference occurs at the entrance of the ring leading to an increased probability for the back scattering and therefore to an appearance of conductance minima. Oscillations with both  $\Phi_0$  and  $\Phi_0/2$  periods were seen simultaneously in the same metal ring<sup>7</sup> for different experimental parameters (temperature, magnetic field range). The halving of the period from  $\Phi_0$  to  $\Phi_0/2$  was also reported in a GaAs quantum ring<sup>8</sup> for different carrier concentrations.

In this paper we present a time-dependent description of the AB effect through the solution of the time-dependent Schrödinger equation for the transport of an electron wave packet through a semiconductor quantum ring<sup>9</sup> in a homogenous magnetic field. The ring is modelled as a two dimensional open structure connected to two leads. The calculations are performed in a basis of Gaussian functions taking into account the finite width of the conduction channel and assuming only lowest sub-

band transport, neglecting inelastic scattering effects. The time dependent picture reveals the magnetic force (called Lorentz force in the following) resulting in a preferential momentum and magnetic field dependent injection of the electron wave packet in one of the junctions of the ring with the incoming and outgoing wires. It is shown that this imbalance injection into the two arms leads to a suppression of the AB oscillations of the packet transmission probability at high magnetic fields, which is similar to the experimentally<sup>8</sup> observed magnetic-field induced decrease of the conductance oscillations in GaAs nanorings. Our results indicate that for circular rings the Lorentz force increases the coupling of the leads to the ring. This changes the transport mechanism from spreading of the charge density maxima formed at the entrance and exit of the ring, which is resonant as function of the incident momentum, to injection of carriers into one of the arms of the ring.

The effect of the magnetic force for scattering experiments has been discussed for biprism diffraction experiments.<sup>10</sup> The envelope of the interference pattern for an electron passing through the flux area is shifted by the magnetic force according to the classical laws due to the Ehrenfest theorem.<sup>10</sup> According to our knowledge the time dependent picture of the effect of the Lorentz force for the AB effect in rings has not been provided so far.

In previous theories<sup>11,12</sup> the scattering matrix approach was used to study the conduction of a one-dimensional ring containing a flux distribution that is inaccessible to electrons, assumed explicitly transport symmetry with respect to the two arms of the ring. Comparable amplitudes for wave function in both arms of the ring were also assumed in the derivation<sup>13</sup> of the multichannel AB conductance formula. The theories of Refs.<sup>[11,12,13]</sup> addressed metals for which, as we discuss below, these

assumptions are justified even if the magnetic field penetrates the two-dimensional ring, since the Lorentz force has a negligible effect on trajectories of electrons travelling with high Fermi velocities. As will be shown in the present paper this is no longer true for the case of semiconductor quantum rings where the Fermi velocity is much smaller.

The monotonic dependence of the injection imbalance as a function of the magnetic field that we obtain contradicts the results of previous time independent calculations of Ref. [14]. According to Ref. [14] the current is injected into the right or left arm of the ring changing periodically with the value of the magnetic field. We disagree with this mechanism and point out that the applied<sup>14</sup> boundary conditions are not well suited for the discussion of the magnetic current injection since the wave function in the output lead is *not* associated with the current flowing out of the ring (see Section V) and the "incident" electron is not necessarily moving towards the ring, so the physics of transport and the role of the magnetic force in it is unclear.

For systems which are invariant with respect to simultaneous inversion of the magnetic field and momentum the probabilities of backscattering<sup>15,16,17</sup> ( $R_{ii}$  to lead  $i$ ) and transmission ( $T_{ij}$  from lead  $i$  to  $j$ ) in a multiterminal device obey the microreversibility<sup>18,19</sup> conditions

$$R_{ii}(B) = R_{ii}(-B) \quad (1)$$

and

$$T_{ij}(B) = T_{ji}(-B). \quad (2)$$

In a two terminal system these relations imply<sup>15,17</sup> that the transmission and reflection probabilities are even functions of the magnetic field ( $B$ ). One of the consequences of this microreversibility is the phase locking<sup>17</sup> of the Aharonov-Bohm oscillations in the conductance of the two-terminal ring which at  $B = 0$  necessarily possesses an extremum. The phase locking contradicts the intuitive expectation that an arbitrary phase shift produced by an asymmetry in the arms of the ring due to a disorder or a quantum well included in one of the arms<sup>20</sup> should be translated into a corresponding shift of the conductance on the flux scale. In the present paper we study the effect of the phase shift produced by a shallow quantum well in one of the arms of the ring. We find that the AB oscillation of the transmission probability is shifted by  $\Phi_0/2$  only when the depth of the well is tuned such that it produces a  $\pi$  phase shift for the maximum of the wave packet in the momentum space. For other depths we find the appearance of minima in the transition probability at integer multiples of  $\Phi_0/2$  which in its turn leads to a halving of the AB period. Therefore a *single* properly chosen phase shifter in one of the ring arms is sufficient to produce the effect of disorder on the AB oscillations.

We have investigated the transport of a wave packet through asymmetric systems, i.e. semicircular quantum

wire and an circular ring with a well in one of the arms, for opposite directions of the magnetic field. We reproduce the microreversibility in the momentum resolved transmission probability, although the processes are complex and have very different kinetics for opposite  $B$  orientations. The reflected part of the packet is independent of the field orientation at any moment in time  $t$  of the simulation but a time delay is observed between the transferred parts of the packet. In general  $T(B, t) \neq T(-B, t)$  but we found that in the limit of large  $t$ , the equality relation  $T(B, t) = T(-B, t)$  holds.

The paper is organized as follows: Section II contains the description of the method. The results are presented in Section III. The results are discussed in Section IV. The Summary and conclusions are given in Section V.

## II. THEORETICAL FORMALISM

### A. Method

We consider an electron confined in the  $(x, y)$  plane with perpendicular magnetic field  $(0, 0, B)$  oriented along the  $z$  axis. The part of the Hamiltonian related to the kinetic energy has the form

$$\begin{aligned} H &= \frac{1}{2m^*} (-i\hbar\nabla + e\mathbf{A})^2 \quad (3) \\ &= -\frac{\hbar^2}{2m^*} \left( \frac{\partial^2}{\partial x^2} + \frac{\partial^2}{\partial y^2} \right) + i\hbar\omega_c y \frac{\partial}{\partial x} + \frac{m^*\omega_c^2}{2} y^2 \end{aligned}$$

with the vector potential taken in the Landau gauge  $\mathbf{A} = (-By, 0, 0)$ . In Eq. (3)  $m^*$  stands for the electron effective mass (we take the GaAs value  $m^* = 0.067m_0$ ). We expand the wave function in a basis of Gaussian functions centered around chosen  $\mathbf{R}_n = (X_n, Y_n)$

$$\Psi(x, y, t) = \sum_n c_n(t) f_n(x, y), \quad (4)$$

with

$$\begin{aligned} f_n(x, y) &= \exp\{-(\mathbf{r} - \mathbf{R}_n)^2/\alpha^2 + \\ &\quad ieB(x - X_n)(y + Y_n)/2\hbar\}/2\sqrt{\pi}\alpha. \quad (5) \end{aligned}$$

Parameter  $\alpha$  expresses the localization of the Gaussian function around point  $\mathbf{R}_n$  and the imaginary part of the exponent is related to the magnetic translation ensuring equivalence of all the points  $\mathbf{R}_n$ , i.e. the gauge invariance. In the finite difference approach special care is required when treating the magnetic field.<sup>21</sup> Substituting expansion (4) into the time dependent Schrödinger equation we obtain a system of linear equations for the time derivative of the coefficients  $c_n(t)$

$$\mathbf{S}\dot{\mathbf{c}}(t) = \mathbf{H}\mathbf{c}(t)/i\hbar, \quad (6)$$

where the elements of the overlap and Hamiltonian matrices are given by  $\mathbf{S}_{kn} = \langle f_k | f_n \rangle$  and  $\mathbf{H}_{kn} = \langle f_k | H | f_n \rangle$ ,

respectively. In the multicenter basis the overlap, kinetic energy matrix elements, and derivatives in general, are evaluated analytically. The entire time evolution of the packet can be found updating the linear coefficients  $c_n$  in each time step according to  $c_n(t + dt) = c_n(t) + \dot{c}_n(t)dt$ . However, this scheme increases the amplitude of the wave function with each time step. For unequal amplitudes of the reflected and transmitted wave packet this effect leads to an artifactual growing imbalance of the scattered and transmitted parts with or without an additional imposed normalization. To overcome this artifact a very small time step of order of the atomic time units ( $\hbar/E_H = 2.4188 \times 10^{-5}$ ps) is needed. More economical solution is provided by the Askar and Cakmak<sup>22</sup> approach where a formal solution of the Schrödinger equation is put in the form  $\Psi(t + dt) - \Psi(t - dt) = (\exp(-idtH) - \exp(idtH))\Psi(t)$ . Using the two first terms of the Taylor series for the time evolution operator gives the scheme  $\Psi(t + dt) = \Psi(t - dt) - 2idtH\Psi(t)$ , which for basis (4) produces the system of linear equations

$$\mathbf{S}\mathbf{c}(t + dt) = \mathbf{S}\mathbf{c}(t - dt) - 2idt\mathbf{H}\mathbf{c}(t). \quad (7)$$

Only the first step in the iteration is calculated with (6), and then one applies the three time-step iteration given by Eq. (7). This scheme is norm-conserving and very stable against the value of the time step. In our calculations the solution obtained for  $dt$  equal to 256 atomic time units cannot be improved any further by decreasing the time step. The system of linear equations (7) is conveniently solved with the LU decomposition method, since the overlap matrix  $\mathbf{S}$  can be decomposed just once, and only the righthand side of the linear system (7) changes with each time step.

## B. Scattering on a one dimensional barrier

To show the efficiency of the method and to illustrate that the wave packet can move smoothly between the centers we performed one-dimensional calculations in the absence of the external magnetic field for an electron tunnelling through a Gaussian barrier given by  $V(x) = V_0 \exp(-x^2/R^2)$  with  $V_0 = 5$  meV and  $R = 2$  nm. We have chosen a Gaussian form for the barrier since our method is not suitable to treat stepwise potentials. This is due to the fact that the Gaussian basis (5) reproduces only wave functions with continuous second derivatives. The initial wave packet is taken as  $\Psi(x, t) = (2/\pi)^{1/4} \exp(-(x - x_0)^2/R_0^2 + iq x) / \sqrt{R_0}$  with  $x_0 = -350$  nm,  $R_0 = 60$  nm and  $q = 0.04/\text{nm}$ . Comparison of the standard finite difference approach with the results of the present method is given in Fig. 1. In the calculations with the Gaussian basis we took  $\alpha = \Delta X$ , where  $\Delta X$  is the distance between homogeneously distributed centers. Calculations were performed in a computational box of 1  $\mu\text{m}$  length. The efficiency of the methods can be directly compared by the required

number of points (centers), i.e., by the size of the linear problem to be solved. Fig. 1 (a) shows the result of the finite-difference simulation for a mesh composed of 201 points. This result is numerically accurate and cannot be visibly improved. Most of the wave packet is reflected from the potential barrier (for the adopted  $q$  the average kinetic energy  $q^2/2m^*$  is equal to 0.9 meV). At the top of the plot (corresponding to long times and large positive  $x$ ) interference fringes coming from the reflection of the transmitted wave packet from the end of the computational box (equivalent to an infinite barrier) is visible. For calculations involving 101 points [Fig. 1(b)] the transmission probability is underestimated and a beating in the interference fringes related to the reflection from the barrier is observed. Finally for 41 points [see Fig. 1(c)] the result is completely unphysical - the wave function becomes entirely localized in the barrier. On the other hand, with the present method, an accuracy comparable to the one of Fig. 1(a), i.e. the exact result, is obtained already for 51 Gaussian functions [Fig. 1(d)]. For 41 Gaussians [Fig. 1(e)] the transmission probability is only slightly overestimated. The physical picture of the process is qualitatively correct also for 31 Gaussians [Fig. 1(f)] although a short-period beating of the probability density is visible. We conclude that usage of the multicenter Gaussian basis allows for a considerable reduction of the numerical complexity of the problem. Obviously, this reduction will be even larger in systems of higher dimensions.

## C. Ring with a wave packet

In this paper we study the transport of electron wave packets through rings of two different shapes: a circular and a diamond ring. The rings considered in the present paper enclose an area of  $132^2\pi$  nm<sup>2</sup>, the value corresponding to the structures studied in the experiment of Fuhrer *et al.*<sup>4</sup> on circular rings. For this area a single flux quantum corresponds to  $B = 75.57$  mT. The shape of the rings is defined by the adopted position of centers ( $\mathbf{R}_n$ ) in functions (5). The centers are chosen along the lines drawn in Fig. 2 with spacings of 20 nm. Parameter  $\alpha$  in functions (5) is set to 28 nm. That choice is equivalent to defining a harmonic oscillator confinement potential with the oscillator energy  $\hbar\omega = 2.9$  meV in the direction perpendicular to the "wires" the rings are made of. We have shown<sup>23</sup> that with the multicenter basis one can reconstruct the eigenfunctions of the angular momentum operator belonging to the ground as well as to excited Landau bands. In our calculations for the circular ring we put 40 centers on the circumference of the ring. For a closed ring structure the time dependence of the movement of the wave packet will therefore be described in a basis of 40 bound eigenfunctions. The incoming and outgoing wires (leads) of the ring are taken along the  $y$ -direction. For the incident wave packet we take one of the Gaussian functions (5), namely the one localized at

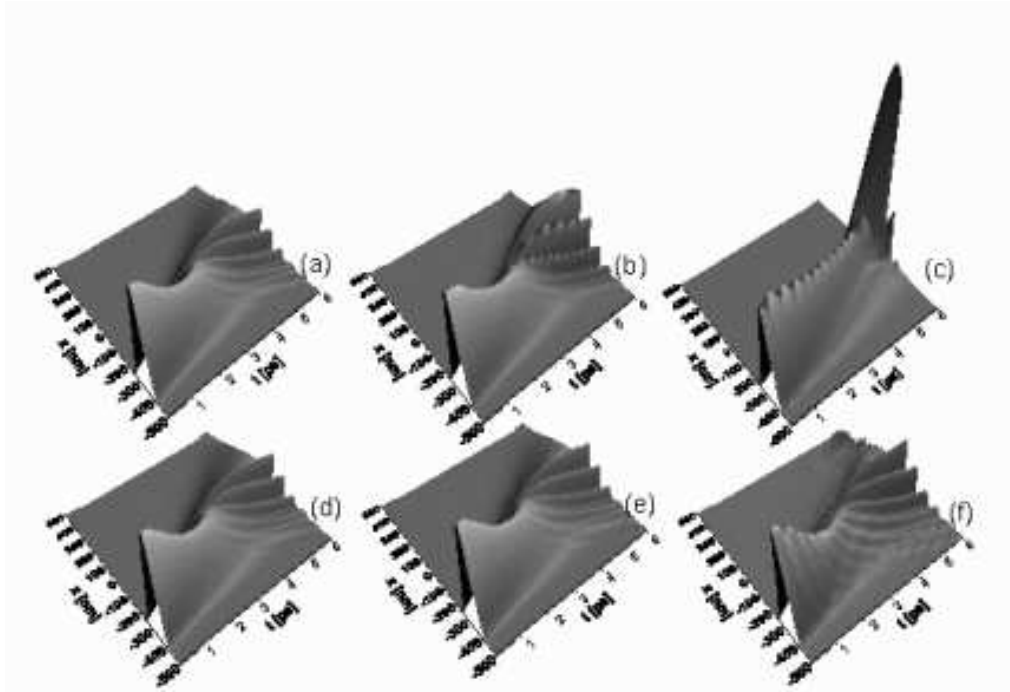


FIG. 1: Time evolution of the density of a one-dimensional wave packet scattered of a Gaussian potential barrier. Plots (a,b,c) show the results of the finite-difference approach using a mesh of 201, 101 and 41 points. Plots (d,e,f) show the result of the present approach with the basis of 51, 41, and 31 Gaussian functions.

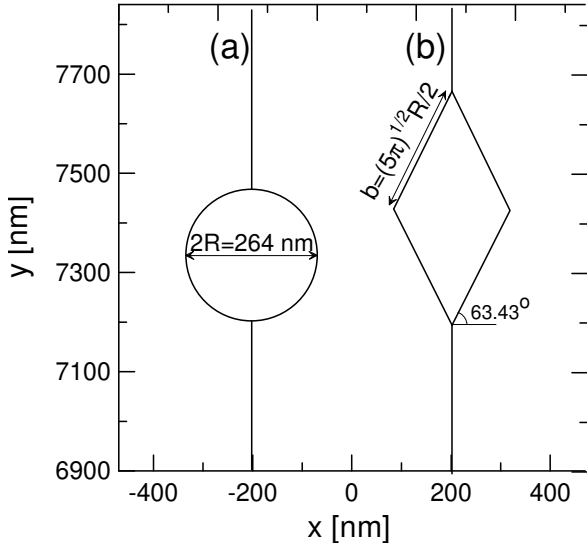


FIG. 2: Geometry and dimensions of the circular (a) and diamond (b) quantum rings studied in the present paper. In the calculations the positions of the centers of the Gaussians (5) are chosen along the drawn lines with a spacing of 20 nm.

the wire at a position  $y_i$ , 200 nm before the entrance of the ring (see Fig. 2) multiplied by a plane wave, i.e.

$$\Psi(x, y, 0) = \exp\left\{-\frac{x^2 + (y - y_i)^2}{\alpha^2} + \frac{ieBx(y + y_i)}{2\hbar} + iqy\right\} / 2\sqrt{\pi}\alpha. \quad (8)$$

This wave function is projected onto the basis (4) and the projection is used as the initial condition for the simulations. The corresponding probability density in wave vector space is given by  $P(k) = \sqrt{\pi}\sigma \exp(-(k - q)^2/\sigma^2)$  with  $\sigma = 0.0505/\text{nm}$ . Note that with the chosen Landau gauge the probability density current vector in the leads, i.e., in the  $y$ -direction is not affected by the vector potential. Therefore, the initial condition for the probability current density is the same for all the magnetic fields (it would not be the case if we took the leads oriented along the  $x$  direction - see Section IV). Let us briefly comment about the movement of the wave packet in the leads. The central part of the packet in the wires moves in the real space according to the Ehrenfest theorem as  $d\langle \mathbf{r} \rangle / dt = \langle \mathbf{p} - e\mathbf{A} \rangle / m^*$ , so in the applied gauge, for the leads oriented along  $y$  direction, the magnetic field has no influence on the movement of the center of the wave packet. The Ehrenfest theorem for the change of the average momentum in time

$$\frac{d\langle \mathbf{p} + e\mathbf{A} \rangle}{dt} = -\frac{e}{m^*} \langle \mathbf{p} + e\mathbf{A} \rangle \times \mathbf{B}, \quad (9)$$

gives for the  $y$ -component the expression

$$\frac{d\langle p_y \rangle}{dt} = \frac{d\langle -i\hbar\partial/\partial y \rangle}{dt} = -\frac{eB}{m^*} \langle i\hbar\frac{\partial}{\partial x} + eyB \rangle. \quad (10)$$

The matrix elements of the operator  $\langle f_m | i\hbar\frac{\partial}{\partial x} + eyB | f_n \rangle$  are zero for  $X_m = X_n$  [see Eq. (5)], so in the leads (oriented parallel to the  $y$  axis) the average value of momentum is conserved. In the leads  $\langle p_x^2 \rangle = 0$  hence the

conservation of  $\langle p_y^2 \rangle$  in the absence of scalar potentials is simply guaranteed by the kinetic energy conservation ( $\langle \mathbf{p}^2 \rangle = \text{const}$ ), which holds for any  $\mathbf{A}$ . We have verified using the Fourier transform analysis that not only  $\langle p_y \rangle$  and  $\langle p_y^2 \rangle$  but the entire momentum distribution remains unchanged in time when the wave packet travels through the leads. Summarizing, in our model the magnetic forces are not active in the leads.

In the present calculations excitations in the direction perpendicular to the wire are not allowed. The simulations are therefore limited to the lowest subband only. Account for higher subbands in the present approach would simply require more centers put side by side on the wires. The entire length of the used computational box is taken up to 23  $\mu\text{m}$  which requires usage of about 1200 Gaussian functions (5). This large (macroscopic) length was necessary to ensure that the reflected and transmitted parts of the wave packets from the ring do not interfere with the reflected wave coming from the ends of the leads before the end of the simulation.

The maximal value of the wave number  $k$  that one can describe in the present method is limited by the spacing between the centers of Gaussian functions. For the adopted value of 20 nm the maximal  $k$  is  $2\pi/40\text{nm} = 0.157/\text{nm}$ . We found for the overlap between the Gaussian (8) and its projection on the basis (4): for  $q = 0.02, 0.05, 0.1, 0.157, \text{ and } 0.2$  [1/nm] the values 0.9999, 0.9983, 0.9413, 0.5, and 0.11967, respectively. The numerical results presented in this paper were obtained for an average value of the momentum  $q = 0.05/\text{nm}$ , which corresponds to an average kinetic energy  $q^2/2m^* = 1.42$  meV and to the classical velocity  $\hbar q/m^* = 86 \times 10^3$  m/s. The average kinetic energy is equal to the Fermi energy ( $E_F = \hbar\pi n/m^*$ ) of the two dimensional electron gas for the lowest subband occupied at the electron concentration  $n = 0.4 \times 10^{11}/\text{cm}^2$ . At the higher energy end of the packet, i.e. for  $k = q + \sigma$ , the kinetic energy 5.36 meV corresponds to  $E_F$  at  $n = 1.6 \times 10^{11}/\text{cm}^2$ .

### III. RESULTS

#### A. Circular ring

Figs. 3-6 show snapshots of the time evolution of the wave packet in a circular quantum ring [see Fig. 2(a)] for 0, 0.5, 4 and 4.5 flux quanta. The contours plots show the charge densities (the scale is the same in all the figures) and the arrows display the probability density vectors calculated as

$$\mathbf{j} = \frac{i\hbar}{2m^*} (\Psi\nabla\Psi^* - \Psi^*\nabla\Psi) + \frac{e}{m^*}\mathbf{A}\Psi\Psi^*. \quad (11)$$

The scale for the probability density vectors is the same in all the plots (b-f) in Figs. 3-6. In parts (a) of Figs. 3-6 the length of the arrows was reduced by 50%.

Plots for  $t = 2.17$  ps [in part (a) of Figs. 3-6] correspond to the moment just before the maximum of the

charge density packet enters the ring. A larger part of the wave packet is scattered back into the injection lead. The interference of the back scattered wave packet and the slower tail of the incoming packet results in the formation of charge density maxima along the injection lead. The plot for  $t = 2.17$  ps with  $\Phi = 0$  [Fig. 3(a)] shows an equal spreading of the wave packet into the left and right ring arms. For  $\Phi = 0$  at  $t = 4.4$  and 6.5 ps [Figs. 3(b,c)] we observe the formation of a *maximum* at the exit region of the ring where left and right circulating parts of the packet meet. Part of the wave packet then leaves into the outgoing wire [Figs. 3(c-f)]. The charge density inside the ring forms several maxima due to the interference of the packets turning right and left [see Figs. 3(c-f)]. Those packets meet at the entrance of the ring and partially leave it following the part of the packet which was back scattered at the beginning of the simulation [see Fig. 3(e)].

Fig. 4 illustrates the propagation of the wave packet when half of a flux quantum ( $B = 0.0378$  T) is applied. For nonzero magnetic field the Lorentz force results in a preferential injection of the packet into the left<sup>24</sup> arm of the ring [see Fig. 4(a)]. For  $\Phi = \Phi_0/2$  the parts of the packet transferred through the left and right arm interfere destructively [Figs. 4(b-f)] leading to a *zero* charge density at the upper exit of the ring. Consequently, no charge is transferred out of the ring at this exit.<sup>25</sup> In fact, the packets are reflected and meet (this time in phase) at the lower entrance of the ring and leave it [Figs. 4(e-f)].

Note that the asymmetry of injection of the wave packet into the left and right arms of the wire increases with magnetic field. Fig. 5 shows the time evolution of the charge density for  $B = 0.302$  T corresponding to 4 flux quanta. Notice the large asymmetry [Fig. 5(a)] in the injection of the wave packet into the two arms of the ring as compared to previous plots [Figs. 3(a) and 4(a)]. This is a consequence of the Lorentz force which directs the wave packet preferentially to the left arm of the ring. We observe also that the wave packet reaches further into the arm as compared to lower magnetic fields. The Lorentz force helps the higher momentum parts of the packet enter into the ring instead being reflected. The force also guides the packet which travels throughout the left arm and exits the ring [Fig. 5(c-d)]. At  $B = 0$  the transport to the wire occurred through spreading of the charge maximum formed at the exit [see Fig. 3(c)].

The results of our simulations for 4.5 flux quanta ( $B = 0.34$  T) are displayed in Fig. 6. In comparison to the case of  $0.5\Phi_0$ , presented in Fig. 4, we see that due to the fact that a larger part of the initial wave packet is transferred along the left arm of the ring results in a non-complete destructive interference at the upper exit. Therefore a part of the packet can exit the ring through the upper lead.

Black solid and blue solid lines in Fig. 7 show the probability to find the electron in the ring (more specifically in the part of the plane described by  $7100 \text{ nm} < y < 7600$  nm) as function of time, for  $\Phi = 0$  and  $\Phi = \Phi_0/2$ , respec-

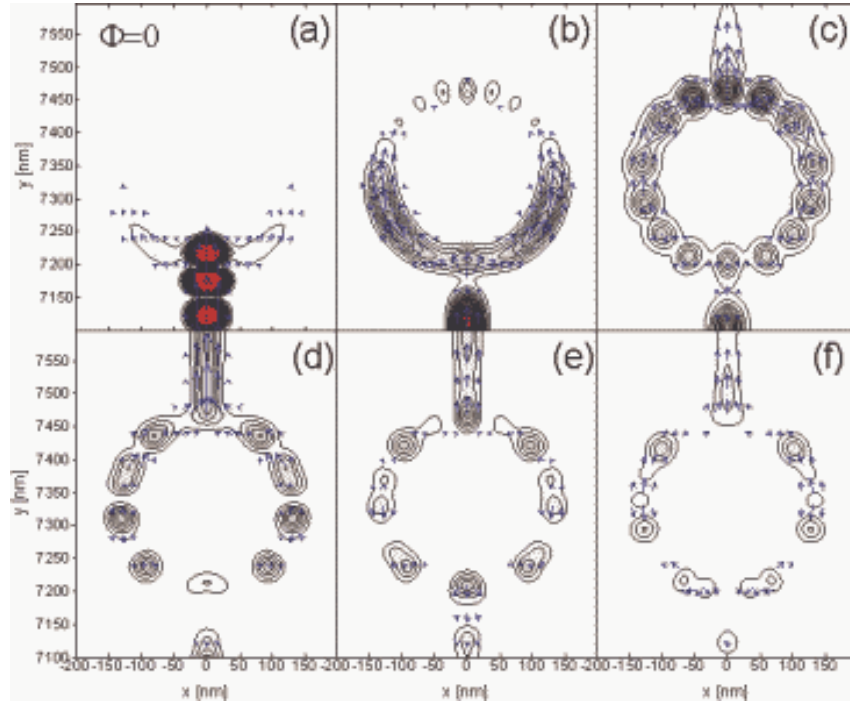


FIG. 3: Charge (contours) and current (vectors) densities for a Gaussian wave packet with kinetic energy  $q^2/2m = 1.42$  meV being transferred through a quantum ring of radius 132 nm for zero magnetic field. Plots (a-f) correspond to  $t = 2.17, 4.35, 6.53, 8.8, 10.88, 13.06$  ps. Scale for the charge and current density is the same in all the plots, with the exception of the current density vectors in (a) which were shortened by a factor of 1/2 with respect to the other plots.

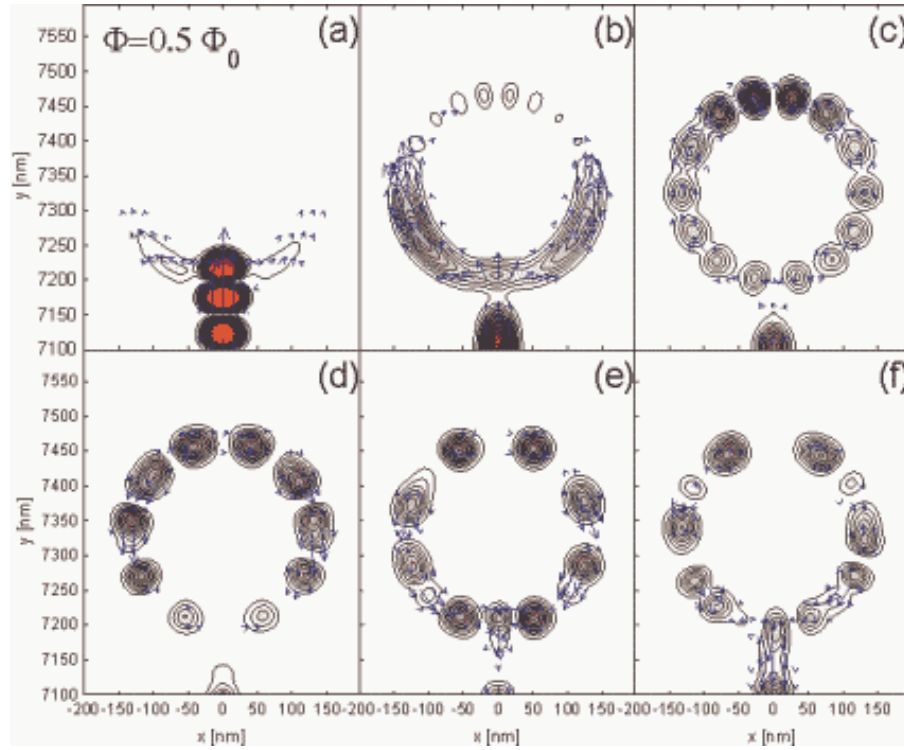


FIG. 4: Same as Fig. 3 but for  $B = 0.0378$  T which corresponds to the flux of the magnetic field through the ring  $\Phi = h/2e = \Phi_0/2$ .

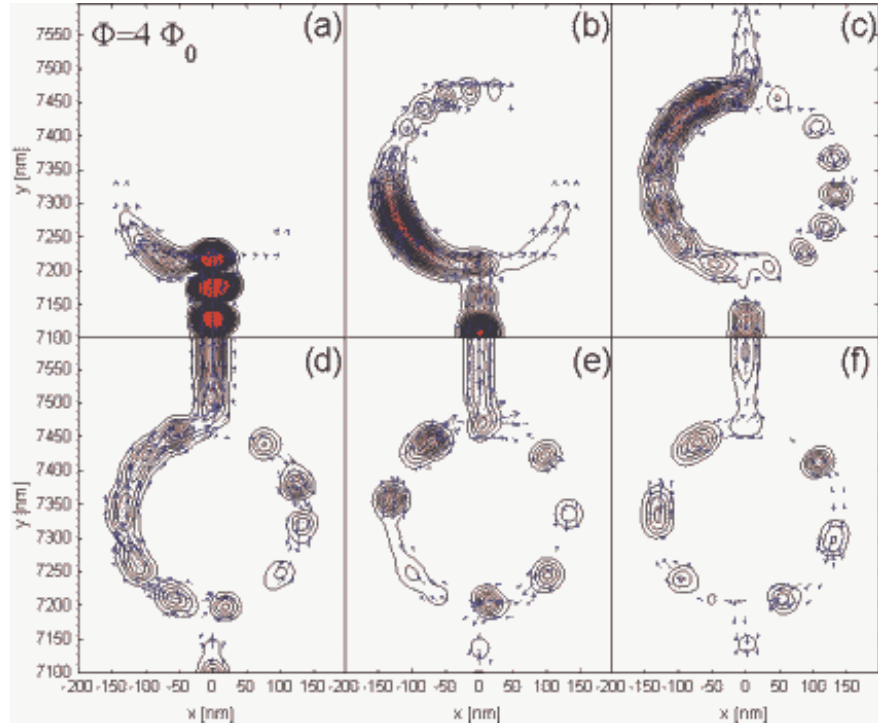


FIG. 5: Same as Fig. 3 but for  $B = 0.302$  T which corresponds to a magnetic flux through the ring of  $\Phi = 4\Phi_0$ .

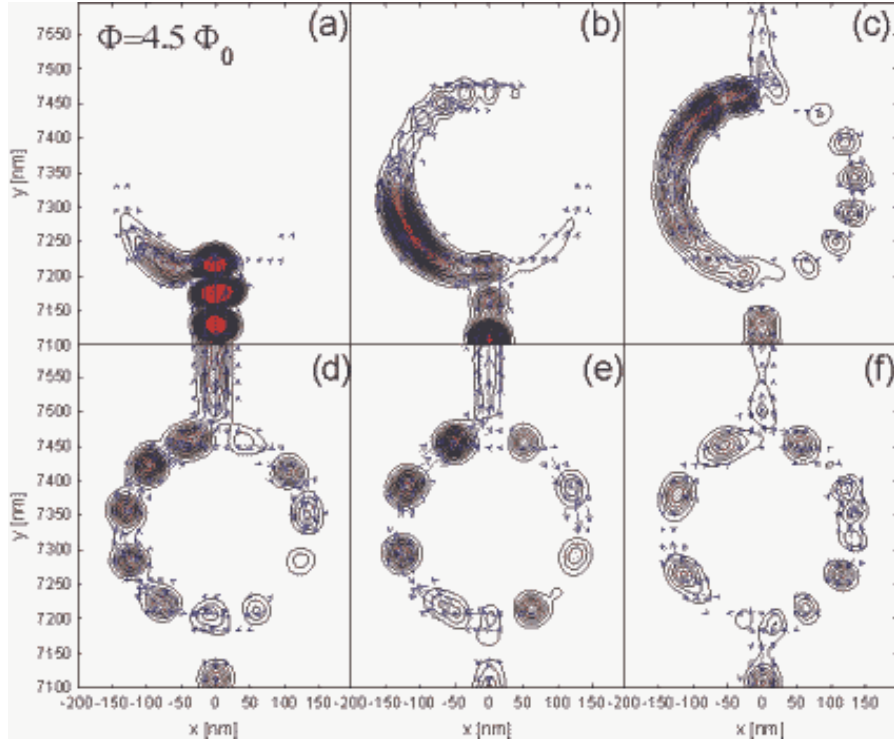


FIG. 6: Same as Fig. 3 but for  $B = 0.34$  T, i.e.  $\Phi = 4.5\Phi_0$ .

tively. Due to the blocking of the transport to the upper lead appearing for  $\Phi = \Phi_0/2$  the electron charge leaves the ring more slowly than in the absence of the magnetic field.

The transmission probability of the wave packet through the circular quantum ring is shown by the solid

line in Fig. 8. This quantity was obtained by integrating the probability density leaving the ring through the upper lead. In contrast to the strictly one-dimensional model with the assumption of equal amplitudes of wave functions entering both arms of the ring as given by the Büttiker single channel formula,<sup>12</sup> we find: 1) that

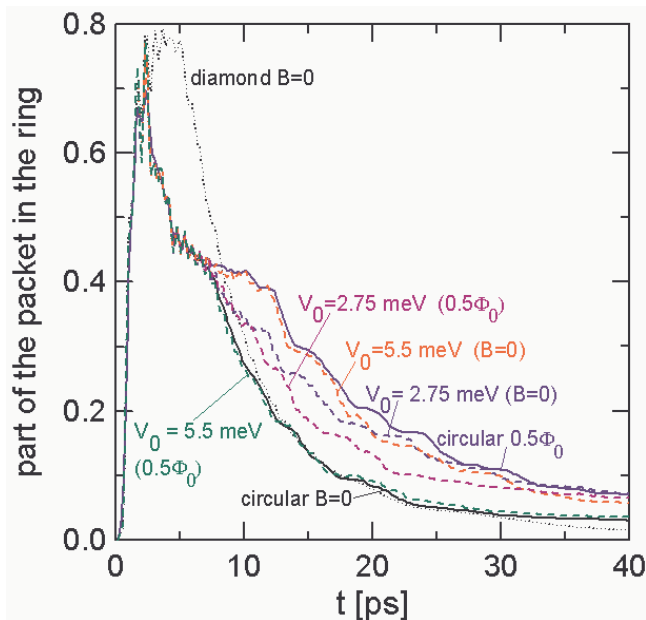


FIG. 7: Probability to find the electron in the ring. Solid lines correspond to the one of a circular ring: the black one to  $\Phi = 0$  and the blue one to  $\Phi = 0.5\Phi_0$ . Dashed lines correspond to a circular quantum well contained in one of the arms of the ring for various depths of the well and different values of the magnetic field (see section III.D). Dotted line shows the probability for the diamond ring without a phase shifter in the absence of the magnetic field (see section III.C).

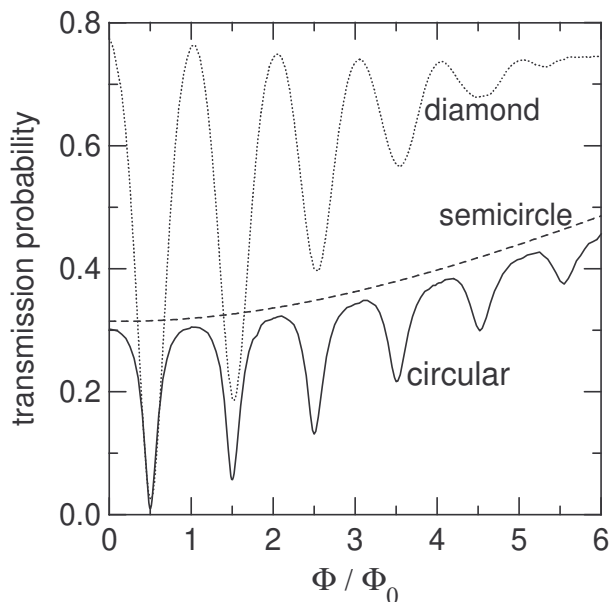


FIG. 8: The transmission probability of the wave packet through the circular (solid line), and diamond (dotted line) quantum rings as function of the flux passing through the ring in units of the flux quantum. The dashed line shows the transmission probability through a wire of a semicircular shape obtained from the circular quantum ring after removal of one of its arms.

the amplitude of the oscillations decreases with magnetic field, and 2) that for half integer fluxes the value of the transmission probability is no longer zero. The decreasing amplitude is due to the growing imbalance in the amount of charge transferred through the left and right arms of the ring which prevents the interference to be completely destructive. The values of the transmission probability maxima and minima are increasing functions of the magnetic field which is a consequence of the guiding behavior of the Lorentz force that eases the entrance and exit of the wave packet.

FIG. 9: Probability density of the transferred wave packet through the circular ring in wave vector space. Black, red, pink, green, and blue lines correspond to 0, 1, 1.5, 7.5 and 8 flux quanta passing through the ring. The dashed line shows the distribution of the initial wave packet. The arrows show the wave vector values equal to  $n/R$  for  $n = 1, 2, \dots, 11$ .

More information on the nature of the electron transport through the ring is obtained by considering the momentum distribution of the transmitted wave packet. This is calculated numerically as the square of the absolute value of the space Fourier transform of the wave function transmitted through the ring. The black solid line in Fig. 9 shows the momentum distribution of the transmitted packet for zero magnetic field. For comparison the momentum distribution of the incident wave packet is plotted by the dashed curve. Notice that there are several pronounced peaks which are approximately equidistant. The origin of these peaks can be understood from the transmission mechanism illustrated in Fig. 3. The momenta which have the highest probability to be transferred (i.e. from the injection to the collection lead) correspond to standing waves in each of the ring arms with maxima of charge density at the entrance and the exit of the ring. This is realized when the phase shift  $k\pi R$  along

each of the arms is equal to an integer ( $n$ ) multiple of  $\pi$  leading to the resonant condition  $k = n/R$ . The distances between the peaks in the momentum distribution of Fig. 3 agree to a precision of 10% with the value  $1/R$ . The actual values of  $n/R$  are marked by arrows in the top of the figure. Position of the momentum peaks for higher values of  $k$  agrees well with these values. For lower momenta the spacing between the peaks increases, as if the resonant length for the slower parts of the packet was shorter.<sup>26</sup> The peaks become wider for lower momentum indicating a less pronounced resonance. The transferred momentum spectrum for one flux quantum (red line in Fig. 8) is very similar to the one for zero magnetic field and the position of the peaks are unaltered. For halves of the flux quanta at lower magnetic fields (see the plot for  $2.5\Phi_0$ ) the nonzero value for the transferred spectra is uniquely due to the injection imbalance preventing the interference at the exit to be completely destructive. The spectrum possesses characteristic double-peak structure in between the maxima for integer flux quanta. The minima between the double peaks correspond to  $k = (n + 1/2)/R$ , which fits the worst it the ring circumference containing an odd number of half wavelengths. Apparently, for this wave vectors the constructive interference at the entrance, due to the AB effect for paths containing a full turn around the ring (see Fig. 4), cancels the effect of the injection imbalance for the transmission probability.

From Fig. 9 we also notice a clear asymmetry in the transferred momentum with respect to its original distribution (see the black solid and dashed lines in Fig. 9). The parts of the wave packet which travel faster have less time to enter into the arms of the ring before they get reflected back at the entrance to the ring into the incoming lead. On the other hand, for higher magnetic field the electron is guided by the Lorentz force into the left arm, when coming from the injection lead, and subsequently to the left, out of the ring to the upper lead (see Fig. 1). This Lorentz-force guided transport does not require the formation of charge density maxima at the entrance and their propagation into and from the ring, which is the reason why the resonant relation no longer holds. The blue curve in Fig. 8 shows the transmitted momentum spectrum for flux equal to  $8\Phi_0$ . We observe two main differences with respect to the  $\Phi = 0$  and  $\Phi = \Phi_0$  results: 1) the gaps between the peaks are filled, and 2) a visibly larger probability of transfer of the fast parts of the packet, which are now directly injected by the Lorentz force into the left arm instead of being reflected at the entrance. Consequently, the spectrum becomes more symmetric and approaches more closely the initial average momentum distribution. At high field for fractional fluxes quanta (see the plot for  $7.5\Phi_0$ ) the minima in the transferred spectrum are shifted towards distinctly nonzero values.

In Table I we put the values of the transmission probability for  $k_1 = 0.0497/\text{nm}$ , corresponding to a sharp minimum of the quantity on halves of the flux quantum (see the green and purple curves in Fig. 9 for  $\Phi = 2.5\Phi_0$

$\Phi/\Phi_0$	$T_{k_1}$	$T_{k_2}$	$T_{k_3}$	$A_{k_1}$	$A_{k_2}$	$A_{k_3}$
0	36.9	45.8	84.5			
0.5	0.02	1.10	0.78	37.6	45.2	83.9
1	38.3	46.8	84.9			
1.5	0.09	9.80	5.80	38.9	39.3	80
2	39.7	51.4	86.7			
2.5	0.80	23.6	16.6	39.7	33	69.1
3	41.3	61.9	84.7			
3.5	3.50	41.2	28.4	43.8	23.6	54.5
4	53.2	67.6	81.0			
4.5	11.3	53.9	38.6	43.3	16.9	43.9
5	56.0	73.9	84.1			
5.5	22.8	66.4	51.3	38.9	9.9	31.5
6	67.5	78.7	81.5			
6.5	40.6	69.2	63.3	30.3	12.6	19.6
7	74.2	84.8	84.3			
7.5	57.8	77.8	70.4	15.6	11.3	12.5
8	72.6	93.4	81.4			
8.5	68.3	76.3	76.5	8.6	12.6	5.4
9	81.2	84.3	82.3			
9.5	76.7	80.2	79.5	4	3.6	1.5
10	80.2	83.2	79.7			

TABLE I: Transmission probability and oscillations amplitude for different values of the flux. First column gives the value of the flux, three next the transmission probability  $T_k$  (in percent), and last three the amplitude of the oscillations  $A_k$  calculated for the fractional flux quanta  $\Phi$  as  $A_k = [T_k(\Phi + \Phi_0/2) + T_k(\Phi - \Phi_0/2)]/2 - T_k(\Phi)$ . The values of the wave vectors are  $k_1 = 0.0497/\text{nm}$ ,  $k_2 = 0.0514/\text{nm}$ ,  $k_3 = 0.0532/\text{nm}$  (see text).

and  $\Phi = 7.5\Phi_0$ ),  $k_3 = 0.0532/\text{nm}$ , corresponding to a maximum of the probability at low integer fluxes (see the black and red curves in Fig. 9 for  $\Phi = 0$  and  $\Phi_0$ ) and for  $k_2 = (k_1 + k_3)/2$ . The results of Fig. 9 and Table I indicate that the overall growth of the transmission probability with the magnetic field observed in Fig. 8 is due to an enhanced transmission of the higher momenta part of the wave packet and to filling 1) the gaps between the resonant peaks at integer fluxes and 2) the minima in the double peak structures at fractional fluxes (see Fig. 9). For  $k_3$  value the amplitude of oscillations decrease monotonically with the flux (see Table I). A deviation from monotonicity is found for  $k_2$ . For  $k_1$  the amplitude of oscillations initially weakly increases with the magnetic field. This is because the gaps between the peaks at integer fluxes are filled faster than the sharp minima at fractional fluxes. Due to the sharpness of the later minima  $k_1$  value is rather nontypical. Eventually, at high magnetic field the AB oscillations are suppressed for all  $k$ .

## B. Diamond ring

Fig. 10 illustrates the time evolution of the wave packet transferred through a diamond quantum ring at  $B = 0$ . In the diamond ring geometry the incoming packet enters the arms of the ring more easily and leaves also more easily the ring to the upper lead. As a consequence, at  $B = 0$  the transmission probability is more than twice larger than for the circular ring (see the dotted line in Fig. 8). For the diamond geometry the transmission probability maxima now only weakly depend on  $\Phi$  since the packet is injected into the arms of the ring and then out of the ring into the upper lead simply by the inertia and not by the Lorentz force. Similarly as in the circular ring the force directs the packet into the left arm of the ring leading to a decrease of the AB oscillations amplitude. In the diamond ring the minima in the oscillations increase much faster with the  $B$ -field as compared to the circular ring. For  $\Phi > 5\Phi_0$  the AB oscillations are no longer observed.

The inertial mechanism of the transfer of the wave packet through the diamond ring is visible also in the Fourier transform of the transmitted wave packet plotted in Fig. 11 for  $B = 0$ . No pronounced resonance pattern similar to the one obtained for the circular ring (see Fig. 9) in the absence of the magnetic field is observed. The transmitted momentum spectrum exhibits an asymmetric shift towards higher momenta with respect to the initial momentum distribution which is opposite to the circular ring case (Fig. 9). The parts of the packet corresponding to higher momenta are now more easily transferred through the diamond ring.

The time dependence of the probability density inside the diamond ring ( $7100 \text{ nm} < y < 7700 \text{ nm}$ ) for  $B = 0$  is shown by the dotted line in Fig. 7. As compared to the circular ring (cf. the black solid line in Fig. 7) a smaller amount of the charge density is immediately reflected to the incoming wire. The electron charge leaves the ring more quickly than for the circular case.

## C. Semicircular wire

We compare the previous result with transport through a semicircular wire that is obtained from the circular ring when one of the arm of the ring is removed. Instead of changing the orientation of the field we considered the two different cases in which one of the arm of the ring are removed. In the following we refer to the wires as "left" or "right" depending on the direction to which the remaining wire is bent.

Snapshots of the simulations are displayed for  $\Phi = 4\Phi_0$  in Fig. 12 (for the left wire) and Fig. 13 (for the right wire). In Fig. 12(a) we see part of the packet injected into the semicircular wire as discussed above in the context of rings. On the other hand, for the right wire at the same moment in time we observe in Fig. 13(a) that the packet is reflected at the point where the wire is bent.

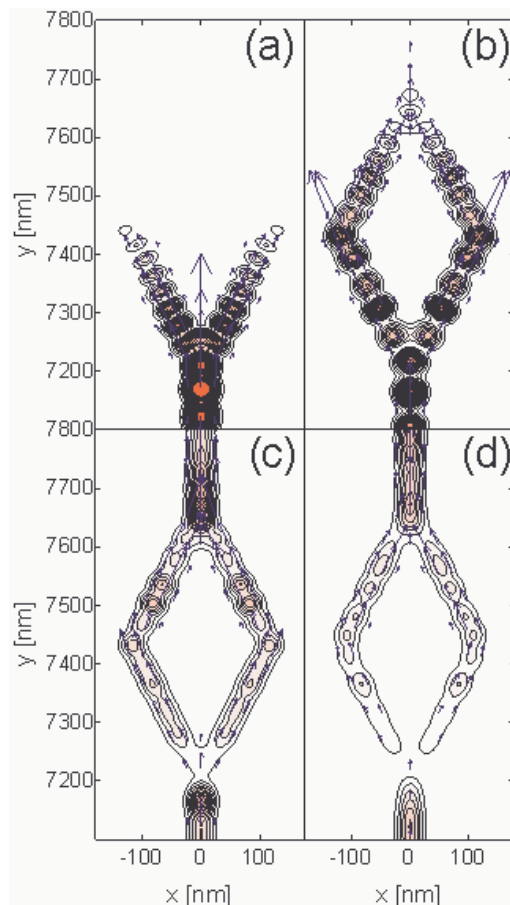


FIG. 10: Same as Fig. 3 but for the diamond ring. Plots (a-d) correspond to  $t = 2.17, 4.35, 6.53, 8.8$  ps, respectively.

The Lorentz-force assisted injection of the charge into the right wire appears only after the reflection of the wave packet, when the velocity of the wave packet changes its direction, i.e. leading to a reversal of the Lorentz force. In the left wire the packet coming to the upper exit is directed to the lead by the Lorentz force [see Fig. 12 (c)] as in the circular ring. On the other hand, for the right wire the packet is ejected out of the semicircular wire when the velocity changes sign [see Fig. 13 (c-d)], similarly as at the entrance, and consequently propagates into the exit lead.

The time dependence of the charge accumulated in the semicircular part of the wire (actually between  $7100 \text{ nm} < y < 7600 \text{ nm}$ , i.e., in the region plotted in Figs. 12 and 13) as well as the probabilities to find the electron below and above the bent are plotted in Fig. 14 for  $\Phi = 10\Phi_0$ . We find the surprising result that the time dependence of the amount of the probability density below the ring is exactly the same for both left and right bent wires. In spite of the time delay of the packet transmitted through the right wire (visible already in Figs. 12 and 13) the transmission probability tend for  $t \rightarrow \infty$  to the same value for both wires for any value of the magnetic field.

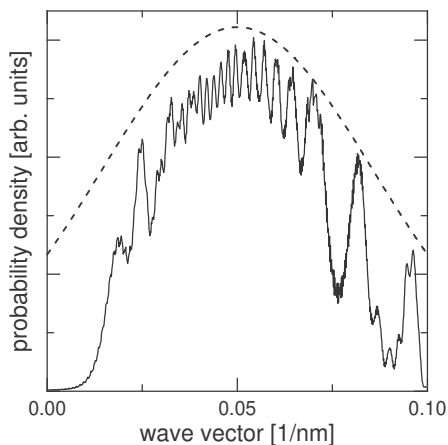


FIG. 11: Probability density of the packet transferred through the diamond ring in wave vector space for  $B = 0$ . The dotted line shows the distribution of the initial wave packet.

The transfer probability of the wave packet through the semicircular wires is plotted by the dashed line in Fig. 8. Note, that it runs parallel to the envelope of the maxima for the circular ring configuration.

The Fourier transform of the wave packets transmitted through the left and right wires calculated for  $\Phi = 4\Phi_0$  is plotted in Fig. 15. Notice that we find an identical spectrum of transferred momentum for both left and right wires. Consequently, the transmission probability invariance with respect to the direction of the magnetic field is preserved.

#### D. Circular ring with a quantum well in the left arm

In order to study the phase perturbation resulting from an asymmetry in the arms of the ring we introduced a shallow Gaussian quantum well in the center of the left arm of the circular ring. For illustrative purposes we solve first the time-independent strictly one-dimensional Schrödinger equation for the transmission through a Gaussian quantum well ( $-V_0 \exp(-x^2/R_d^2)$ ). In the calculations we fixed  $R_d = \alpha = 28$  nm. We take a particle coming from negative  $x$  with wave function far away to the right of the well  $\exp(iqx)$ . Sufficiently far to the left of the well the wave function is  $C \exp(iqx) + D \exp(-iqx)$ , where  $C$  and  $D$  are the amplitudes of the incident and reflected plane waves. The transmission probability is given by  $1/|C|^2$  and the phase shift acquired by the wave function passing through the well is simply given by the argument of  $C^*$ . Fig. 16 presents the transmission probability and the phase shift as function of the wave vector. The shallow well potential is transparent for wave vectors larger than  $0.025/\text{nm}$ , for which the transmission probability is nearly one and only the phase is changed with respect to the  $V_0 = 0$

(no quantum well) case. The phase shifts are continuous functions of the wave vector. The phase shift for  $k = 0.05/\text{nm}$  (maximum of the probability density used in the time-dependent simulations) is close to  $\pi/4$ ,  $\pi/2$  and  $\pi$  for  $V_0 = 1$ ,  $2.75$  and  $5.5$  meV, respectively. The absence of a pronounced Ramsauer effect, i.e., peaks of the transmission probability when the incident electron energy is aligned with a resonance above the barrier is due to the smoothness of the barrier and not to its shallow depth.

In the time dependent simulations for the ring structure we introduce a quantum well described by the potential

$$V(x, y) = -V_0 \exp[-((x - X_l)^2 + (y - Y_l)^2) / R_d^2], \quad (12)$$

where  $(X_l, Y_l)$  is the center of the basis function (5) situated in the middle of the left arm of the ring. The transmission probability of the wave packet is plotted as a function of the well depth  $V_0$  in Fig. 17 (a) for different values of the flux. The dependence of the probability on the depth of the well is due to the phase shift acquired by that part of the wave packet which passes through the arm of the ring containing the dot. For integer multiples of the flux quantum the transmission probability has a minimum when the phase shift for the maximum of the wave packet in momentum space is equal to  $\pi$ , which is achieved at  $V_0 = 5.5$  meV, as obtained in the previous one-dimensional calculation (see Fig. 16) for  $q = 0.05/\text{nm}$  – the average momentum value of the studied wave packet. Fig. 17(b) shows the comparison of the momentum distribution of the transferred part of the packet for  $V_0 = 0$  and  $V_0 = 5.5$  meV at  $\Phi = 0$ . The phase shift acquired in the dot and the destructive interference at the exit to the lead removes the central part of the wave packet in momentum space. For fluxes equal to halves of the flux quantum the quantum well in one of the arms has the opposite effect on the transmission probability since it *compensates* for the  $\pi$  shift produced by the AB effect. As a consequence the probability increases [see dashed lines in Fig. 17 (a)] when  $V_0$  is increased from 0, and is maximal for  $V_0 = 5.5$  meV where the compensation of the AB phase shift is obtained. The central part of the transferred momentum spectrum at  $\Phi = 0.5\Phi_0$  for  $V_0 = 5.5$  meV [red line in Fig. 17 (c)] is similar to  $V_0 = 0$  in the absence of the magnetic field [compare black line in Fig. 17 (b)]. Note, that the transmission probability as a function of  $V_0$  plotted in Fig. 17 (a) is not an ideally smooth function. The changing slope of the curve is due to switching on and off the resonances in the transmitted momentum spectrum.

The magnetic field dependence of the transfer probability for  $V_0 = 5.5$  meV is plotted in Fig. 18 by the blue line. The transfer probability possess maxima at the magnetic fields corresponding to halves of the flux quanta passing through the ring, for which the Aharonov-Bohm effect compensates for the dot related  $\pi$  shift. The transfer probability through a quantum dot with  $V_0 = 4$  meV is plotted by the green curve in Fig. 18. By analogy to the results for  $V_0 = 0$  and  $V_0 = 5.5$  meV one could

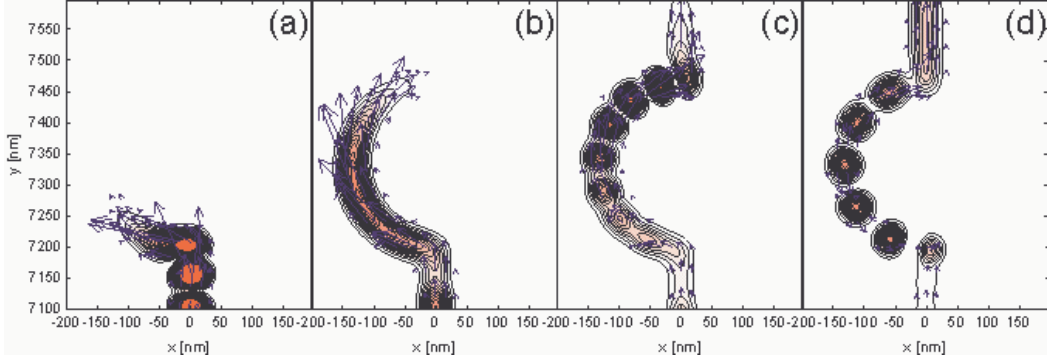


FIG. 12: Same as Fig. 3 but now for a semicircular wire where the right arm of the circular ring is removed at  $B = 0.302$  T ( $\Phi = 4\Phi_0$ ). Plots (a-d) correspond to  $t = 2.17, 4.35, 6.53, 8.8$  ps, respectively.

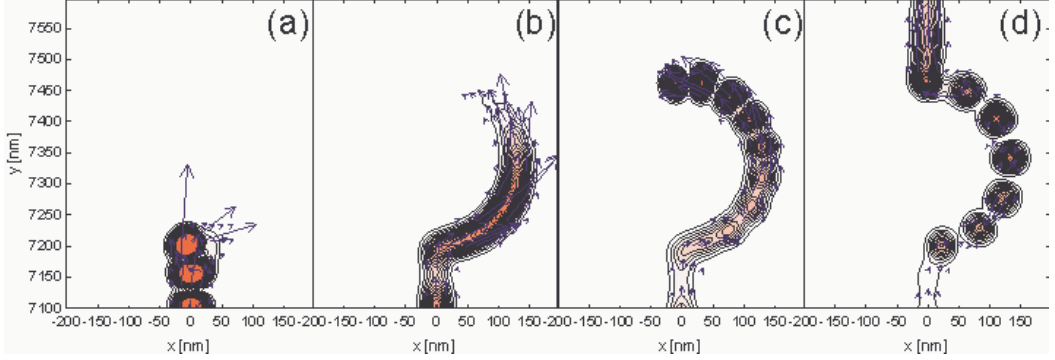


FIG. 13: Same as Fig. 12 but now for the case in which the left arm of the ring is removed.

expect a similar behavior with minima spaced by  $\Phi_0$  but shifted on the flux scale. However, this is not what we observe since it would violate the even symmetry of the two-terminal device properties as a function of the external field. For  $V_0 = 4$  meV the transmission probability develops shallow minima at odd multiples of the half flux quantum. At these values of the magnetic field the waves with  $k$  values of the maximum of the wave packet in  $k$ -space do not meet exactly in phase at the upper exit from the wire, but on the other hand, the rotating left and right parts of the packet meet exactly in phase at the entrance. Both these factors decrease the transfer probability of the packet producing the discussed minima. The depth of the probability minima for both the odd and even multiples of  $\Phi_0/2$  decrease with increasing flux. The shallow minima at odd multiples of  $\Phi_0/2$  are not visible for  $|\Phi| > 3\Phi_0$ . At  $V_0 = 2.75$  meV the phase shift for the maximum of the wave packet ( $q = 0.05/\text{nm}$ ) is about  $\pi/2$  (see Fig. 16). The minima at the even and odd multiples of  $\Phi_0/2$  acquire similar depth (see red curve in Fig. 18). As a consequence the transmission probability exhibits oscillations with a period of half of the flux quantum. For  $V_0 = 1$  meV the  $T(\Phi)$  (see the purple curve in Fig. 18) becomes similar to the symmetric ring  $V_0 = 0$  case with the exception of shallow minima appearing at integer multiples of the flux quantum.

The time dependence of the probability to find the electron in the ring for  $V = 5.5$  meV was plotted in Fig. 7 by the green and red dashed curves for  $\Phi = 0$  and  $\Phi = 0.5\Phi_0$ , respectively. The  $\Phi = 0$  plot is similar to the one obtained for the ring without the quantum well in the arm but for half of the flux quantum (cf. blue solid line in Fig. 7). However, for the ring containing the well in the absence of the magnetic field, the packet leaves the ring more quickly since the transfer to the upper lead is less effectively blocked because of the  $k$  dependence of the well related phase shift. A magnetic field corresponding to half of the flux quantum almost exactly cancels the influence of the quantum well when considering the probability to find the electron in the ring (compare the green dashed line and the solid black line in Fig. 7). The time dependence of the probability to find the electron in the ring for  $V = 2.75$  meV is plotted for  $\Phi = 0$  and  $\Phi = \Phi_0/2$  fluxes with dashed blue and purple curves in Fig. 7, respectively. The magnetic field corresponding to half the flux quantum has a much weaker influence on the time dependence of the probability than in the case of  $V_0 = 5.5$  meV since it does not fully compensate for the phase shift acquired by the central part of the packet passing through the quantum well.

The time dependence of the probability density in the ring and in the leads is plotted in Fig. 19 for  $V_0 = 2.75$

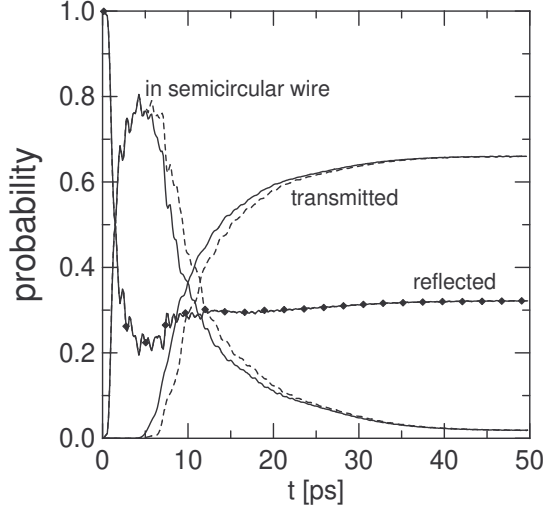


FIG. 14: Probability to find the electron inside the semicircular wire ( $7100 \text{ nm} < y < 7600 \text{ nm}$ ) above ( $y > 7600 \text{ nm}$ ) and below it ( $y < 7100 \text{ nm}$ ) as function of time for  $\Phi = 10\Phi_0$ . The solid (dashed) lines show the results for the right (left) wire. The reflected probability density for the right semicircular wire is marked by the dots.

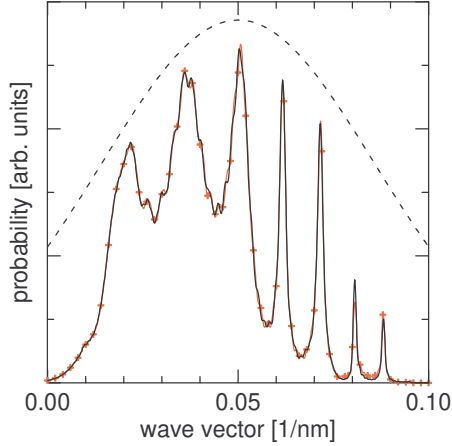


FIG. 15: Probability density of the transferred wave packet through the semicircular wires bent left (red curve with red crosses) and right (black curve) when 4 flux quanta are passing through the ring. The dotted line shows the distribution of the initial wave packet.

meV and fluxes  $0, \pm\Phi_0/20$  and  $\pm\Phi_0/3$  (the latter corresponds to a local maximum of the transfer probability, see Fig. 18). Application of a negative flux compensates partly for the phase shift produced by the Gaussian quantum well. Consequently, a larger part of the wave packet is directly (i.e. in the first round of the wave packet density around the ring) transferred to the upper lead. In contrast, the positive flux increases the value of the relative phase shift from  $\pi/2$  (for  $q = 0.05/\text{nm}$ ) towards  $\pi$ . The part of the wave packet transferred to the upper lead at the beginning of the simulation is reduced with

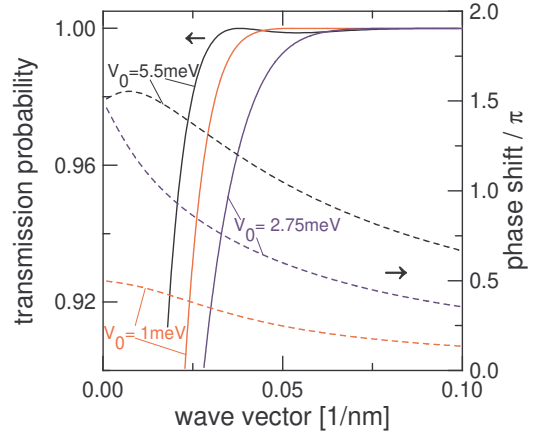


FIG. 16: Transmission probability (solid lines) and the phase shift (dotted lines) as function of the wave vector for a Gaussian quantum well of width 28 nm and different depth  $V_0$ .

respect to the  $B = 0$  case. However, the transfer probability turns out to be independent of the sign of the flux (see the large  $t$  limit for the blue and red curves as well as for green and purple curves). The time delay between the transmitted part of the packet for opposite fluxes is much more pronounced than for the semicircular wires (compare with Fig. 14). Equal value of the transferred packet is obtained only after several rotations of the packet inside the ring. Similarly as for semicircular wires, the amount of the reflected probability as a function of time is independent of the magnetic field orientation.

#### IV. DISCUSSION

Our results for circular rings, both with (see Fig. 18) and without (see Figs. 8) a phase shifting quantum well, exhibit Lorentz-force related overall increase of transmission probability with magnetic field accompanied by a decreasing amplitude of the oscillations. This is in qualitative agreement with the magnetoconductance measurements<sup>8</sup> performed on GaAs/AlGaAs quantum rings (see Fig. 1 of Ref. [8]). The calculated overall increase of the transmission probability depends on the shape (for instance, it is not observed for the diamond ring) and on the momentum (it is not necessarily observed for a fixed value of wave vector even in the circular ring - see Table I) but the decrease of the oscillations amplitude is obtained as a general feature. The obtained decreasing amplitude of AB oscillations with magnetic field was also observed in GaAs / AlGaAs nanorings formed by an AFM tip<sup>4</sup> (see the ring current plot in Fig. 2(c) of Ref. [4]) and in the AB interferometer (see Fig. 3(a) of Ref. [20]). A suppression of the periodic magnetoresistance oscillations was also reported in Ref. [3]. As we showed, the decreasing amplitude can be understood by the imbalance of the charge passing through the arms of the ring and does not necessarily involve an increase of the

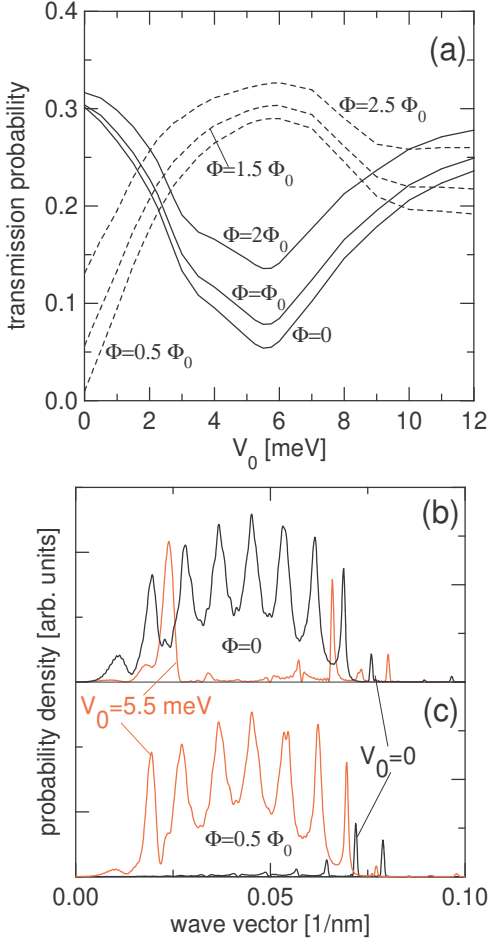


FIG. 17: (a) Transmission probability of the wave packet through a circular ring with a Gaussian quantum well [Eq. 12] in the left arm as a function of the depth of the well  $V_0$ . Values for fluxes equal to integer flux quanta are plotted with solid and for half flux quanta with dashed lines. (b) The transferred momentum distribution for  $V_0 = 0$  (black line) and  $V_0 = 5.5$  meV (red line) at  $\Phi = 0$ . (c) Same as (b) but now for  $\Phi = 0.5\Phi_0$ .

inelastic scattering phase coherence loss by the external magnetic field or scattering to higher subbands.

In order to be of significant importance for the imbalance, the Lorentz force has to be able to deflect the electron trajectories at the entrance and at the exit leads of the ring. The classical formula for the radius of an electron in a magnetic field  $R = m^*V/eB$  (for the average  $q = 0.05/\text{nm}$  taken in our calculations  $R = 32.9 \text{ nm T}/B$ ) indicates that the effect will be smaller for fast electrons since the radius will not fit into the width of the junction. This feature was actually confirmed in the context of Fig. 9. In metals the Fermi energies are of order eV which compares to meV in a two-dimensional electron gas in GaAs with electron densities<sup>4,8</sup> of order of  $10^{11}\text{cm}^{-2}$ . Consequently, in Au rings<sup>2</sup> in which both the electron effective mass ( $\sim m_0$ ) and the Fermi velocity ( $1.4 \times 10^6 \text{ m/s}$ ) are about 15 times

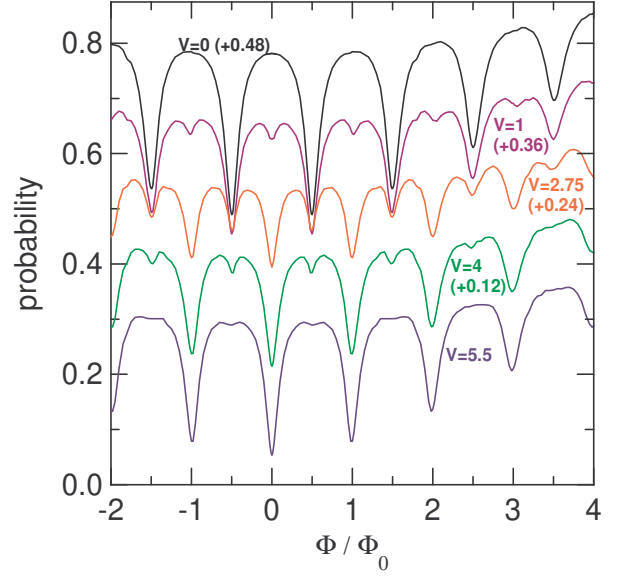


FIG. 18: Probability of transmission of the wave packet through a circular ring with a Gaussian quantum well [Eq. 12] in the left arm as a function of the magnetic field flux for well depths:  $V_0 = 5.5$  meV (blue line), 4 meV (green line), 2.75 meV (red line), 1 meV (green line) and 0 (black line). Lines for  $V_0 = 4$  meV, 2.75 meV, 1 meV and 0 have been shifted for clarity by +0.12, +0.24, +0.36 and +0.48, respectively.

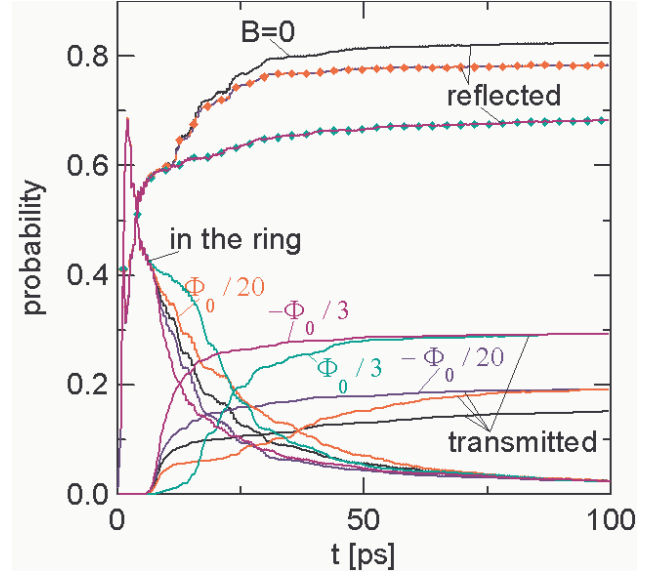


FIG. 19: The probability to find the electron in the ring, before (reflected) and after (transmitted) the ring for a Gaussian quantum well of depth  $V_0 = 2.75$  meV in the left arm of the circular ring for zero magnetic field (black lines), and for fluxes  $-\Phi_0/20$  (blue lines),  $+\Phi_0/20$  (red lines),  $-\Phi_0/3$  (purple lines) and  $+\Phi_0/3$  (green lines). Symbols show the part of the wave packet before the ring, i.e. reflected, for positive value of the flux.

larger than the effective mass and the velocity considered in the present paper, the AB oscillations pertain up to 8 T covering as much as  $10^4$  flux quanta  $\Phi_0$ . Recently, AB oscillations in a semiconductor quantum ring<sup>5</sup> pertaining to large fluxes were observed in a device with electrostatic tunnel barriers in both arms of the ring. In the experiment<sup>5</sup> the barriers were tuned to have equal transmission which can compensate for the Lorentz force effect described in the present paper.

Our calculations neglect inelastic scattering and therefore correspond, in essence to 0K temperature. For 0K the electrons passing through the ring have a well defined Fermi level and are monoenergetic. In our calculations we made a superposition of plane waves corresponding to different energies in order to form the wave packet. However, the information about specific Fermi wave vectors could be extracted by the Fourier analysis. The decrease of the amplitude shown for a specific momentum (see the end of section III. A) shows that the magnetic force effect is present also in the time independent problem and is not only applicable to wave packet kinetics.

The imbalance of the current through the arms of the ring as due to the magnetic field was previously<sup>14</sup> obtained through the time independent simulation. However as mentioned in the introduction, dependence of the current found in Ref. [14] is very different from the one obtained in the present paper, since the current imbalance between the arms of the ring is predicted<sup>14</sup> to change periodically with the magnetic field. The same gauge was applied<sup>14</sup> as in the present paper but the leads were taken parallel to the  $x$  axis near  $y = 0$ . The Hamiltonian eigenstates in the leads were calculated for separable wave function as  $g_k(x, y) = \exp(ikx)f_k(y)$ , where  $f_k$  is the eigenfunction of the one-dimensional Hamiltonian  $H = -\frac{\hbar^2}{2m^*} \frac{d^2}{dy^2} + \frac{1}{2m^*} (\hbar k - m^* \omega_c y)^2$  with zero boundary conditions on the wall, i.e., for  $y = \pm d/2$ . The probability density current in the  $x$ -direction for eigenstate  $g_k$  is given by  $j_x(y) = |f(y)|^2 \left( \frac{\hbar k}{m} - \omega_c y \right)$ . At high magnetic field for low wave vectors<sup>14</sup> (when  $\omega_c \gg \hbar k/m^*$ ) the current  $j_x(y)$  has the opposite orientation at the top ( $y > 0$ ) and bottom ( $y < 0$ ) sides of both the injection and the extraction lead. The physics behind the calculations<sup>14</sup> is therefore only clear for zero magnetic field for which the current is proportional to the wave vector  $k$  and for which the Landauer conductance theory in form presented in Ref. [14] is correct. Otherwise, one simply cannot tell from which lead the electron is coming and to which it is going. At high field for the single channel transport the authors obtain a transmission probability as a bi-value function equal to zero for odd multiples of  $\Phi_0/2$  and 1 for other fluxes (see Fig. 13 for  $\epsilon = 20$  of Ref. [14]). According to our calculations there is no physical reason which would lead to a strict vanishing of the single-channel conductance at high magnetic field penetrating the arms of the two-dimensional quantum ring.

In the presence of magnetic forces the tunnelling of the

electron wave packet through the left and right wires described in the present paper are distinctly different physical processes. Indeed, the time dependence of the probability density transmitted through the semicircular wire clearly exhibits this asymmetry in the time delay of the transmission probability. The time delay is related to the velocity dependent direction of the Lorentz force injecting the wave packet into the bent part of the wire. The delay for the back scattered part of the packet is absent. Therefore, for the rings the discussed imbalance of the wave packet entering the left and right arms (see Fig. 5 and 6) is uniquely due to the time delay between the entering of the wave packet to the ring and its reflection from the rings inner wall at the entrance. The packet is injected to the left arm before it can be (after reflection) injected to the right arm of the ring.

## V. CONCLUSION AND SUMMARY

We have solved the time dependent Schrödinger equation for a Gaussian electron wave packet passing through a quantum ring in the presence of a homogenous external magnetic field. In contrast to previous strictly one-dimensional time-independent theories our results indicate that the amplitude of the Aharonov-Bohm oscillations for semiconductor quantum rings decrease with external magnetic field due to the Lorentz force action on the moving electron. In circular quantum rings the magnetic field changes the mechanism of transport, i.e., increasing the strength of the coupling of the ring to the leads with increasing magnetic field. The momentum resonances in the tunnelling at low magnetic field resemble the formation of a quasi-bound temporary state localized in the ring. At high magnetic field the tunnelling becomes guided by the Lorentz force. In structures which are nonsymmetric with respect to its junctions to the upper and lower leads (as discussed for the semicircular wire and a quantum ring with a phase shifting quantum well) the Lorentz force introduces differences in the physics of the tunnelling processes for opposite orientations of the magnetic field. The sign of the magnetic field changes the time spent by the electron in the ring, but keeps the transmission probability independent of the orientation as agrees with the fundamental symmetry relations for a two terminal device. The reflected part of the packet is independent of the sign of the flux at any time. The presence of the asymmetry in one of the ring arms leads to a  $\pi$  shift of the oscillations of the wave packet transmission probability or to halving of the period of its Aharonov-Bohm oscillations.

**Acknowledgments** We are grateful to T. Ihn and K. Ensslin for helpful discussions and to A. Sadreev for email correspondence. This research was supported by the Flemish Science Foundation (FWO-V1) and the Belgian Science Policy, B.S. is supported by the EC Marie Curie IEF project MEIF-CT-2004-500157.

- 
- <sup>1</sup> Y. Aharonov and D. Bohm, Phys. Rev. **115**, 485 (1959).
- <sup>2</sup> R.A. Webb, S. Washburn, C.P. Umbach, and R.B. Laibowitz, Phys. Rev. Lett. **54**, 2696 (1985).
- <sup>3</sup> G. Timp, A.M. Chang, J.E. Cunningham, T.Y. Chang, P. Mankiewich, R. Behringer, and R.E. Howard, Phys. Rev. Lett. **58**, 2814 (1987).
- <sup>4</sup> A. Fuhrer, S. Lüscher, T. Ihn, T. Heinzel, K. Ensslin, W. Wegscheider, and M. Bichler, Nature (London) **413**, 822 (2001).
- <sup>5</sup> W. G. van der Wiel, Yu. V. Nazarov, S. De Franceschi, T. Fujisawa, J. M. Elzerman, E. W. G. M. Huizeling, S. Tarucha, and L. P. Kouwenhoven, Phys. Rev. B **67**, 033307 (2003).
- <sup>6</sup> B.L. Al'tshuler, A.G. Aronov, B.Z. Spivak, D. Yu. Sharvin, and Yu. V. Sharvin, JETP Lett. **35**, 588 (1982).
- <sup>7</sup> V. Chandrasekhar, M.J. Rooks, S. Wind, and D.E. Prober, Phys. Rev. Lett. **55**, 1610 (1985).
- <sup>8</sup> S. Pedersen, A.E. Hansen, A. Kristensen, C.B. Sorensen, and P.E. Lindelof, Phys. Rev. B **61**, 5457 (2000).
- <sup>9</sup> S. Viefers, P. Koskinen, P. Singa Deo, and M. Manninen, Physica E (Amsterdam) **21**, 1 (2004).
- <sup>10</sup> S. Olariu and I.I. Popescu, Rev. Mod. Phys. **57**, 339 (1985) and references therein.
- <sup>11</sup> Y. Gefen, Y. Imry, and M. Ya. Azbel, Phys. Rev. Lett. **52** (1984).
- <sup>12</sup> M. Büttiker, Y. Imry, and M. Ya Azbel, Phys. Rev. A **30** 1982 (1984).
- <sup>13</sup> M. Büttiker, Y. Imry, R. Landauer, and S. Pinhas, Phys. Rev. B **31**, 6207 (1985).
- <sup>14</sup> K. N. Pichugin and A.F. Sadreev, Phys. Rev. B **56** 9662 (1997).
- <sup>15</sup> M. Büttiker, Phys. Rev. Lett. **57**, 1761 (1986).
- <sup>16</sup> M. Büttiker, Phys. Rev. B **38**, 9375 (1988).
- <sup>17</sup> A. L. Yeyati and M. Büttiker, Phys. Rev. B **52** R14360 (1995).
- <sup>18</sup> L. Onsager, Phys. Rev. B **38**, 2265 (1931).
- <sup>19</sup> H.B.G. Casimir, Rev. Mod. Phys. **17**, 343 (1945).
- <sup>20</sup> A. Yacoby, M. Heiblum, D. Mahalu, and H. Shtrikman, Phys. Rev. Lett. **74**, 4047 (1995).
- <sup>21</sup> R. Kato, Y. Enomoto, S. Maekawa, Phys. Rev. B **44**, 6916 (1991); *ibid* **47**, 8016 (1993).
- <sup>22</sup> A. Askar and A. C. Cakmak, J. Chem. Phys. **68**, 2794 (1978).
- <sup>23</sup> B. Szafran, F.M. Peeters, S. Bednarek, and J. Adamowski, Phys. Rev B **69**, 125344 (2004).
- <sup>24</sup> Note that a single function of type (5) gives a lowest Landau level wave function (see Ref. [<sup>23</sup>]) with the probability density current field  $(\omega_c/2) \exp(-e|B|((x-X)^2 + (y-Y)^2)/2\hbar)(-(y-Y), (x-X))$ , turning counterclockwise (for  $B > 0$ ), i.e., with the direction of the current turning left around the center of the Landau orbit.
- <sup>25</sup> Actually the transport probability for this field is about 0.8%, but the transferred packets are below the threshold of plotted charge densities. The nonzero value is due to the asymmetric injection discussed further in the text.
- <sup>26</sup> The resonances appear when the antinodes of the wave functions are formed near the junctions. For lower  $k$  (longer wavelengths) the effective width of the junction is larger.